Accepted Manuscript

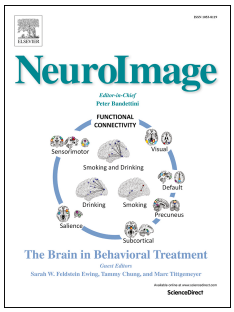

Can anomalous diffusion models in magnetic resonance imaging be used to characterise white matter tissue microstructure?

Qiang Yu, David Reutens, Viktor Vegh

PII: S1053-8119(18)30262-3

DOI: 10.1016/j.neuroimage.2018.03.052

Reference: YNIMG 14821

To appear in: *NeuroImage*

Received Date: 4 December 2017

Revised Date: 13 March 2018

Accepted Date: 22 March 2018

Please cite this article as: Yu, Q., Reutens, D., Vegh, V., Can anomalous diffusion models in magnetic resonance imaging be used to characterise white matter tissue microstructure?, *NeuroImage* (2018), doi: 10.1016/j.neuroimage.2018.03.052.

Can anomalous diffusion models in magnetic resonance imaging be used to characterise white matter tissue microstructure?

Qiang Yu, David Reutens and Viktor Vegh*

Centre for Advanced Imaging, the University of Queensland, Brisbane, Queensland, Australia

Short running title: Probing of tissue microstructure via anomalous diffusion models

*Corresponding author:

Viktor Vegh

Centre for Advanced Imaging

Building 57

University of Queensland

Brisbane, QLD, 4072

Australia

E-mail: v.vegh@uq.edu.au

Phone: +61 7 3365 4100

Fax: +61 7 3346 0330

Word count for body of text: 8335

Abstract:

Purpose: During the time window of diffusion weighted magnetic resonance imaging experiments (DW-MRI), water diffusion in tissue appears to be anomalous as a transient effect, with a mean squared displacement that is not a linear function of time. A number of statistical models have been proposed to describe water diffusion in tissue, and parameters describing anomalous as well as Gaussian diffusion have previously been related to measures of tissue microstructure such as mean axon radius. We analysed the relationship between white matter tissue characteristics and parameters of existing statistical diffusion models.

Methods: A white matter tissue model (ActiveAx) was used to generate multiple *b*-value diffusion-weighted magnetic resonance imaging signals. The following models were evaluated to fit the diffusion signal: 1) Gaussian models - 1a) mono-exponential decay and 1b) bi-exponential decay; 2) Anomalous diffusion models - 2a) stretched exponential, 2b) continuous time random walk and 2c) space fractional Bloch-Torrey equation. We identified the best candidate model based on the relationship between the diffusion-derived parameters and mean axon radius and axial diffusivity, and applied it to the *in vivo* DW-MRI data acquired at 7.0 T from five healthy participants to estimate the same selected tissue characteristics. Differences between simulation parameters and fitted parameters were used to assess accuracy and *in vivo* findings were compared to previously reported observations.

Results: The space fractional Bloch-Torrey model was found to be the best candidate in characterising white matter on the base of the ActiveAx simulated DW-MRI data. Moreover, parameters of the space fractional Bloch-Torrey model were sensitive to mean axon radius and axial diffusivity and exhibited low noise sensitivity based on simulations. We also found spatial variations in the model parameter β to reflect changes in mean axon radius across the mid-sagittal plane of the corpus callosum.

Conclusion: Simulations have been used to define how the parameters of the most common statistical magnetic resonance imaging diffusion models relate to axon radius and diffusivity. The space fractional Bloch-Torrey equation was identified as the best model for the characterisation of axon radius and diffusivity. This model allows changes in mean axon radius and diffusivity to be inferred from spatially resolved maps of model parameters.

Key words: Magnetic resonance imaging, anomalous diffusion, tissue microstructure, white matter, simulation, mathematical modelling

1. Introduction

The Bloch equation describes the dynamic relationship between externally applied magnetic fields and internal sample relaxation times for homogeneous materials with a single spin component such as water protons (Abragam, 2011). However, in the presence perturbations such as chemical exchange and diffusion processes, the Bloch equation has to be implemented to describe properly the magnetization behavior. In nuclear magnetic resonance (NMR) spectroscopy, the Bloch-McConnell equations were developed to describe the NMR signal in the presence of chemical exchange (Hansen and Led, 2003), whereas in 1956 the Bloch-Torrey equations were introduced (Torrey, 1956), in which effects on the magnetic resonance imaging (MRI) signal due to diffusion are considered (Abragam, 2011). These models were based on classical calculus and the underlying assumption that the scale at which measurements are taken and the scale at which changes occur are similar.

The last few decades have seen the development of NMR models based on fractional calculus (Bhalekar et al., 2011; De Santis et al., 2011; Magin et al., 2008; Palombo et al., 2012; Petráš, 2011; Qin et al., 2017a, 2017b; Xu et al., 2017a, 2017b) in parallel with the application of fractional calculus in other fields, e.g. digital image processing (Pu et al., 2010; Yu et al., 2015), physics (Hilfer, 2000; Metzler and Klafter, 2000; Zaslavsky, 2002), engineering (Yu et al., 2008), finance (Scalas et al., 2000), and hydrology (Hosking, 1984). Such models may be better suited to problems in which the scales of measurement and of the underlying phenomenon are mismatched (Metzler and Klafter, 2000). This is the case in MRI, where microstructural influences affect the signal measured at the millimetre scale. The integer derivatives used in classically derived equations only act locally, whereas non-local physical behaviors can be captured through the use of fractional order derivatives, i.e. equations derived using fractional calculus can take into account what is happening within a certain vicinity governed by the fractional derivative (Kilbas et al., 2006). Essentially, the non-integer order derivative in a fractional model defines the ‘memory’ or ‘hereditary’ properties of the physical system. Fractional models tend to have a larger number of parameters as they allow additional information about the system to be represented. A number of studies have used fractional models to investigate tissue using MRI data (Magin et al., 2008, 2009; Petráš, 2011; Qin et al., 2017a, 2017b; Zhou et al., 2010).

The Bloch-Torrey equations have been used to calculate mean diffusivity, fractional anisotropy, radial diffusivity and axial diffusivity of biological tissue from data obtained using diffusion weighted imaging. The mono-exponential model solves the Bloch-Torrey equations under the assumption of isotropic diffusion (Torrey, 1956). However, it is not well-suited to describe diffusion data of the brain, compared to more complex models that either include additional mono-exponential terms or use a stretched exponential approximation. MRI researchers usually assume an averaging process over a large number of spins that, while useful at millimetre scale resolution, may not be suitable if the influence of smaller structures on water diffusion in the human brain is to be accounted for (Metzler and Klafter, 2000). To date it has been assumed that the mean-squared displacement of water diffusion remains Gaussian in the restricted diffusion signal compartment when the gradient field is applied as part of a diffusion-weighted magnetic resonance imaging (DW-MRI) scan. However, during individual measurements, diffusion takes place on a time scale over which boundary and interface

interactions can occur (Mori and Zhang, 2006; Price, 2009), and the Gaussian mean-squared displacement assumption does not hold (Sen, 2003; Upadhyaya et al., 2001). Consequently, it has been suggested that diffusion in tissue is anomalous by nature and that, as a corollary, diffusion in image voxels containing heterogeneous signal compartments is anomalous (Kimmich, 2002; Köpf et al., 1998).

We used transient anomalous diffusion models to investigate the biological tissues, wherein for long diffusion times diffusion becomes Gaussian (Novikov et al., 2016). Recently, several different fractional calculus models have been proposed to represent anomalous diffusion in MRI experiments:

(i) Stretched exponential (STRETCHED): an empirical extension of the mono-exponential model without an underlying theory wherein an additional parameter is used to shape the decay of the function (Bennett et al., 2003).

(ii) Continuous time random walk (CTRW): a spatio-temporal model based on the diffusion equation (Metzler and Klafter, 2000), which incorporates heterogeneity of intra-voxel diffusion in time (model parameter α) and space (model parameter β). This model was first introduced by Palombo et al. (2011) derived using an effective physical approach and later by Magin et al. (2013) and Ingo et al. (2015) derived using mathematical approaches.

(iii) Space fractional Bloch-Torrey equation (FBTE): the solution to the Bloch-Torrey equation when the derivatives have been generalized to fractional order and considered the special case when only the spatial derivatives are fractional (Magin et al., 2008).

The STRETCHED and CTRW models were originally developed to characterise anomalous diffusion in DW-MRI, and the resulting parametric maps were used to study differences between grey and white matter. Magin et al. (2008) proposed the space and time fractional Bloch-Torrey equation. The solution obtained from the FBTE model with the Stejskal-Tanner gradient was used to fit diffusion-weighted images acquired for a normal human brain. In a follow-up study Zhou et al. extended their work to *b*-values as high as 4700 s/mm^2 (Zhou et al., 2010) and applied the twice-refocused spin echo diffusion sequence (Gao et al., 2011). We have also used the FBTE model to probe white matter microstructure, focussing on the estimation of mean axon radius and volume fraction in the human corpus callosum (Yu et al., 2017). However, a systematic evaluation of how anomalous diffusion models relate to specific white matter characteristics has not been conducted to date. Such information may help in the development on new biomarkers of brain diseases.

To evaluate the utility of diffusion models to probe white matter microstructure with MRI, we undertook a simulation study using an extensively used white matter tissue model, ActiveAx (Alexander et al., 2010) to generate the diffusion signal. ActiveAx, which incorporates axon radius, diffusivity, volume fraction and gradient directions, is the most general model of DW-MRI signal formation in white matter. It considers water compartments for intra- and extra cellular spaces, cerebrospinal fluid and stationary water and allows the effects of changes in white matter model parameters (i.e. mean axon radius and diffusivity) to be simulated. Here, we evaluate the sensitivity of classical and anomalous diffusion model

parameters to mean axon radius and diffusivity. ActiveAx was used for signal generation. Five diffusion models (MONO, BI, STRETCHED, CTRW and FBTE) were fitted to the diffusion signal and the relationship between individual model parameters and ActiveAx parameter settings was examined. We then spatially resolved parameters of the best model in data acquired for the corpus callosum in the *in vivo* MRI setting.

2. Materials and methods

ActiveAx was used to generate a synthetic diffusion signal with multiple *b*-values, upon which we based our model analyses. After identifying the best candidate model for characterising white matter microstructure, we collected 7 T MRI diffusion-weighted data from five healthy participants. Using the *in vivo* data from the corpus callosum of each participant, we sought to confirm trends predicted by the simulations.

2.1 White matter model (ActiveAx)

The ActiveAx model of water diffusion in white matter proposed by Alexander et al. (2010) has four signal compartments, denoted as S_{ic}, S_{ec}, S_{csf} and S_{tw}, each contributing to the MRI signal of an image voxel.

S_{ic}: Intracellular restricted diffusion is represented by cylinders following the Gaussian phase distribution approximation. In the case of narrow gradient pulses and when the diffusion time is much longer than the gradient pulse duration (van Gelderen et al., 1994), the signal is given by:

$$S_{\mathrm{ic}} = S_0 e^{-\gamma^2 G^2 \delta^2 R^2}, \tag{1}$$

where R is the representative intracellular radius following a two-parameter gamma distribution (Barazany et al., 2009), γ is the gyromagnetic ratio, G is the magnetic field gradient and δ is the gradient pulse duration. The meaning of long diffusion time should be interpreted in the context of restricted boundaries defined by R. The longer the diffusion time, the larger the amount of interaction with boundaries. Therefore, when R is small, shorter diffusion times can be used, and when R is large, longer diffusion times should be used. The weights of radius are given by a gamma function:

$$w_i\left(R_i; k, \theta\right) = \frac{R_i^{k-1} e^{-\frac{R_i}{\theta}}}{\theta^k \Gamma\left(k\right)}, \tag{2}$$

where w_i is the weight for the cellular signal with intracellular radius R_i, k (>0) and θ (>0) are two parameters of the gamma distribution, and $\Gamma(k)$ is the gamma function evaluated at k (Kilbas et al., 2006).

S_{ec}: Hindered diffusion in extracellular space following anisotropic Gaussian distributed displacements (Basser et al., 1994). The signal from this compartment is given by:

$$S_{ec} = S_0 e^{-b\mathbf{D}_{\mathrm{eff}}}, \tag{3}$$

where $\mathbf{D}_{\mathbf{eff}} = d^T \mathbf{D}^*_{eff} d$ and d is the gradient direction $d = (d_1, d_2, d_3)^T$, $\mathbf{D}^*_{eff} = (D_{//} - D_{\perp}) nn^T + D_{\perp} I$ and n is the vector representing fibre direction, $D_{//}$ is the diffusivity along n, $D_{\perp}$ is the apparent diffusivity perpendicular to n, and I is the three dimensional identity matrix. The intrinsic diffusivity inside the cylinders for model S_{ic} is the same as $D_{//}$. Szafer et al. proposed a simple tortuosity model (Szafer et al., 1995):

$$D_{\perp} = D_{//}(1 - v) \ , \tag{4}$$

where $v = f_{ic}/(f_{ic}+f_{ec})$ and f_{ic} and f_{ec} are the volume fractions of S_{ic} and S_{ec}.

S_{csf}: The partial volume effect due to CSF is governed by isotropic Gaussian displacements (Barazany et al., 2009):

$$S_{csf} = S_0 e^{-bD_{csf}} \ , \tag{5}$$

where D_{csf} = 3 µm^2/ms representing diffusion in the CSF.

S_{tw}: Stationary water from subcellular structures, which is not attenuated by the diffusion weighting:

$$S_{tw} = S_0 \ . \tag{6}$$

With the above four compartments, and assuming chemical exchange of the water molecule exchange does not occur between compartments, the total diffusion MRI signal is given by:

$$S^* = f_{ic} S_{ic} + f_{ec} S_{ec} + f_{csf} S_{csf} + f_{tw} S_{tw} \ , \tag{7}$$

where f represents volume fractions, $0 \le f_{ic}, f_{ec}, f_{csf}, f_{tw} \le 1$ and $f_{ic} + f_{ec} + f_{csf} + f_{tw} = 1$.

2.2 ActiveAx parameter settings

We performed the simulations with the following values for axial diffusivity, D_i = 0.6 µm^2/ms, D_{ii} = 1.0 µm^2/ms, D_{iii} = 1.4 µm^2/ms and D_{iv} = 1.8 µm^2/ms. These were chosen to reflect previously published results of 1.61 µm^2/ms (Rimkus et al., 2013) or 1.7 µm^2/ms (Alexander et al., 2010) for *in vivo* human brain, 1.4 µm^2/ms for *in vivo* rat (Barazany et al., 2009) or mouse (Sun et al., 2006b) brain, 1.0 µm^2/ms (Assaf et al., 2004) for excised pig spinal cord tissue, 0.74 µm^2/ms (Sun et al., 2006a) for the mouse optic nerve *ex vivo*, and 0.6 µm^2/ms (Alexander et al., 2010) for fixed monkey brain.

As measurement times with DW-MRI lie between 10 ms and 100 ms (Mori and Zhang, 2006), we tested three diffusion time regimes: SHORT (Δ = 10 ms) with δ = 5 ms, MEDIUM (Δ = 50 ms) with δ = 10 ms and LONG (Δ = 100 ms) with δ = 20 ms. Note, these choices of δ and Δ have been made in view of practical limitations associated with collecting data using human MRI scanners. The MEDIUM and LONG diffusion time regimes satisfy both the narrow pulse ($\delta << \Delta$) and long diffusion approximations (e.g. when D = 1.0 µm^2/ms and maximum R = 5 µm, then in Δ = 50ms a mean displacement of around 7 µm is achieved, which is sufficient for boundary restrictions to occur, an assumption for (1)). In the case of the SHORT diffusion time regime, assumptions used to generate (1) may not be satisfied for large R, however they may be satisfied for small R.

Volume fraction f_{ic} in the tissue model was set as $f_{ic} = 0.2$, based on mean volume fraction results of 0.14 and 0.26 for the human corpus callosum, *ex vivo* and *in vivo* respectively (Yu et al., 2017). The other three volume fractions in the tissue model were set as $f_{ec} = 0.7$, $f_{csf} = f_{tw} = 0.05$ (Yu et al., 2017).

Intracellular radius R_i in the intracellular compartment S_{ic} ranged between 0.1 µm to 20 µm in steps of 0.1 µm.Parameters of the gamma distribution were set to $k = 100$ and θ was varied between 0.005 and 0.05 in steps of 0.005. This allowed us to achieve a mean intracellular radius (R) of 0.5 µm to 5 µm in steps of 0.5 µm.

The same *b*-values and gradient directions used in a previous *in vivo* experiment (refer to Yu et al., 2017) were used to generate the ActiveAx diffusion weighted MRI signal, which was then converted to trace data. The MRI signal without diffusion weighting, S_0, was arbitrarily fixed at 1,000. We tested the performance of each model without and with the addition of Rician noise at SNR levels of 15 dB and 10 dB, where the 15 dB level (about 30 when expressed as signal over noise and not in dB; NORMAL SNR) corresponds to the SNR of routinely acquired diffusion signals in MRI, and the 10 dB level (also 10 when expressed as signal over noise and not in dB; LOW SNR) corresponds to a low SNR regime. At each SNR level, simulations were repeated 1,000 times with different random Rician noise to evaluate model performance.

2.3 Diffusion models

Mono-exponential diffusion (MONO) model

The MONO model is given by (Le Bihan, 2007):

$$S(b) = S_0 e^{-bD} \quad , \tag{8}$$

where S_0 is the MRI signal without diffusion weighting, D is the diffusion coefficient, $b = \gamma^2 G^2 \delta^2 (\Delta - \delta / 3)$ is the *b*-value and Δ is the time from the beginning of the first gradient pulse to the beginning of the second gradient pulse. Diffusion MRI signal loss deviates from mono-exponential decay in many biological tissues, particularly at high *b*-values, for example, $b > 1500$ s/mm^2 (Le Bihan, 2007).

Bi-exponential diffusion (BI) model

The BI model assumes that there are two distinct diffusion compartments within each voxel (Clark and Le Bihan, 2000):

$$S(b) = S_0 \left[v e^{-bD_1} + (1 - v)\, \mathrm{e}^{-bD_2} \right] , \tag{9}$$

where v is the volume fraction of the fast diffusing compartment and D_1 and D_2 are the diffusion coefficients for the fast and slow diffusion compartments. This model assumes that water exchanges slowly between the two compartments during the diffusion measurement time. The first term has been associated with the extracellular compartment and the second term with the intracellular compartment.

Stretched exponential (STRETCHED) model

Bennett et al. (2003) postulate that non-mono-exponential decay results from a continuum of diffusion compartments leading them to propose a STRETCHED model:

$$S(b) = S_0 e^{-b^{\alpha} D^{\alpha}}, \tag{10}$$

where D is the distributed diffusion coefficient which is independent of b-value, and α in (0,1] is the exponent describing the width of the decay curve. The model was used to characterize water diffusion rates in the cortex and fitted signal evolution better than the bi-exponential model in 20% of voxels.

Continuous time random walk (CTRW) model

The CTRW model is based on a generalization of random walk theory (Metzler and Klafter, 2000). In heterogeneous materials characterized by tortuous and porous geometries, the motion of diffusing particles is anomalous (Capuani et al., 2013; Palombo et al., 2011; Ingo et al., 2015; Karaman et al., 2016a; Kilbas et al., 2006), and the jump distance and jump waiting time are no longer constrained by a Gaussian distribution but follow asymptotic power law distributions. The following assumed relations could be used to study sub-diffusive processes (Capuani et al., 2013; Palombo et al., 2011):

$$\mathrm{S}(k,t) = S_0 \exp\left(-D_{\alpha} k^2 t^{\alpha}\right) \text{ when } k^2 \gg 1/\left(D_{\alpha} t^{\alpha}\right), \tag{11}$$

where D_{α} is a generalized diffusion constant, $k = \gamma G \delta / (2\pi)$ and α in (0, 1). In addition, the following relations could be used to investigate super-diffusive processes (Capuani et al., 2013; Palombo et al., 2011):

$$\mathrm{S}(k,t) = S_0 \exp\left(-D^{2\mu} k^{2\mu} t\right), \tag{12}$$

where $D^{2\mu}$ is a generalized diffusion constant and μ in (0, 1). Furthermore, the diffusion-weighted signal attenuation in the CTRW model with the Stejskal-Tanner gradient can be described using the Mittag-Leffler function as (Karaman et al., 2016a):

$$S(b) = S_0 E_{\alpha}\left(-b^{\beta} D_m^{\beta}\right), \tag{13}$$

where the dimensionless parameter α is the diffusion waiting time, which theoretically reflects the temporal heterogeneity faced by water molecules. Parameter β is the diffusion jump length reflecting spatial heterogeneity of the tissue. E_{α} is the single parameter Mittag-Leffler function (Kilbas et al., 2006). D_m is termed the anomalous diffusion coefficient and has units of μm^2/ms. It is defined as $D_m^{\beta} = D_{1,2} \frac{\tau^{1-\alpha}}{\mu^{2-2\beta}} \left(\Delta - \frac{\delta}{3}\right)^{\alpha-\beta}$ where $D_{1,2}$ is the nominal diffusion coefficient with units of mm^2/s, and α in (0, 1) and β in (0, 1).

Note that two different types of diffusion data have to be collected to fit (11) and (12). For the former, data should be obtained using a pulse field gradient sequence and Δ has to be changed when *G* is fixed to be able to resolve a value for α in (11). For the latter, data is obtained using a pulse field gradient sequence wherein *G* is varied and Δ is fixed to be able to fit parameter μ in (12). Modern diffusion-weighted human MRI sequences allow for changes in the *b*-value through changes in *G* within one acquisition, however they do not allow for multiple values of Δ within one sequence. Our work focuses on models which are applicable with the acquisition of multiple *b*-value data within one acquisition, as this approach is practical and data can be acquired in a reasonable amount of time. Therefore, we opted to study the utility of (13), which essentially has the same form as (12), i.e. let $D^{2\mu} = D_m^{\beta}$ and $k^{2\mu}t = b^{\beta}$, and can be applied with multiple *b*-value data.

Space Fractional Bloch-Torrey equation (FBTE)

In this model, diffusion-weighted signal attenuation with the Stejskal-Tanner gradient is given by (Magin et al., 2008):

$$S(b) = S_0 \exp\left[-D\mu^{2(\beta-1)} b^{\beta} \left(\Delta - \frac{\delta}{3} \right)^{-\beta} \left(\Delta - \frac{2\beta - 1}{2\beta + 1}\delta \right) \right], \qquad (14)$$

where *D* is the diffusion coefficient, $\mu^{2(\beta-1)}$ is the fractional order space constant needed to preserve units, and β is the spatial heterogeneity index in (0, 1). We have developed numerical approaches for solving FBTE and proved the stability and convergence of the methods (Song et al., 2014; Yu et al., 2012, 2013a, 2013b). Equation (14) has also been used to fit diffusion-weighted data acquired for a normal human brain allowing construction of *D*, β and μ maps (Magin et al., 2008).

2.4 Diffusion model parameter estimation and evaluation

Fig. 1 shows the signal attenuations at three different mean axon radii (*R* = 0.5 µm, 2.5 µm and 5 µm) for different ActiveAx axial diffusivities and three different diffusion time regimes in the absence of noise. Fig. 2 provides a schematic of how model parameters were estimated. For simulated diffusion signals generated using ActiveAx and different combinations of mean axon radius and axial diffusivity, a non-linear least squares fitting algorithm (Levenberg-Marquardt) in MATLAB ® was used to estimate parameters in different diffusion models.

Figure 1: The signal attenuations at three different mean axon radii (*R* = 0.5 µm, 2.5 µm and 5 µm) and SHORT, MEDIUM and LONG diffusion times, for four different ActiveAx axial diffusivities ($D_{//}$).

Figure 2: The process involved in generating diffusion model parameters is outlined. The ⊗ symbol signifies the generation of fitted signal and diffusion model parameters using the diffusion and tissue models respectively. The flowchart shows an example using the FBTE diffusion model with mean axon radius of *R* = 5 µm and axial diffusivity of *D* = 1.0 µm^2/ms in the tissue model. An example of the noisy signal is provided.

We used mean relative error (MRE) to evaluate how well each model fitted the simulated signal. The MRE is the mean of the summed absolute error divided by the magnitude of the signal, where the absolute error is the magnitude of the difference between the fitted and simulated signals. The corrected Akaike Information Criterion (AICc) was used to select the best model (Anderson et al., 1994). The AICc incorporates a correction for finite sample sizes. The linear regression model, $Y = mX+c$, was used to measure how well the diffusion coefficient *(Y)* in each model predicted axial diffusivity in the tissue model (*X*). Here, *m* is the slope of the linear regression line and *c* is the intercept. The coefficient of determination, r^2 (between 0 and 1) was used to measure goodness-of-fit of the calculated linear regression model. An r^2 of 1 indicates that a perfect fit was achieved. A lager value for r^2 leads to better one-to-one mapping between set and calculated diffusivities, and *m* denotes the relationship between the two. Note, *m* reflects how the axial diffusivity set in ActiveAx can be interpreted in terms of the diffusivity calculated using each of the models. We also evaluated the sensitivity of model parameters to changes in each of the tissue model parameters.

We used the following criteria to determine the best model:

A. *Diffusivity* - the diffusion coefficient in the model should reflect axial diffusivities set in the tissue model. In our study, the best linear regression model is one which has a high goodness-of-fit (r^2), i.e. the axial diffusivity set is as directly related as possible to the measured value, and an intercept (*c*) close to zero, i.e. an axial diffusivity of zero maps to a mean diffusivity of zero. The slope *m* plays a lesser role as it increases or decreases the mapped values.

B. *Non-intersection of curves* - the plots of the model parameter versus mean axon radius for different diffusivities should not intersect. We state the percentage of parameters for which non-intersection is the case.

C. *One-to-one mapping* - the model parameter should have a one-to-one mapping (not including *D* as we expect it to be linear) to ActiveAx tissue model parameters. We state the percentage of parameters in which this is the case.

D. *Wide range of sensitivity to tissue microstructure parameters* - the plots of the model parameter versus mean axon radius should be affected evenly by diffusivity across a wide range. We state the percentage of parameters in which this is the case (i.e. there is equidistant spacing between curves as a function of diffusivity).

The noiseless simulation data were used as the benchmark in the analysis for noise sensitivity. The SNR = 15 (NORMAL SNR) and SNR = 10 (LOW SNR) data sets were fitted with all models and the change in model parameters with the addition of noise was measured. Our goal here was to identify the model which has parameters least affected by noise.

2.5 *In vivo* human MRI data

The *in vivo* human brain study was approved by the University of Queensland's Human Research Ethics Committee, Brisbane, Australia. Written consent was provided by each participant prior to MRI scanning. Diffusion-weighted images were acquired in five healthy human male participants (5 males aged 33-66 years with mean age 43.6 year) on a 7 T

whole body MRI research scanner (Siemens Healthcare, Erlangen, Germany) with a maximum gradient strength of 70 mT/m at a slew rate of 200 mT/m/ms. Each participant underwent a 20 minute imaging session (approximately 5 minutes for pre-scans, 7 minutes for structure data and 8 minutes for collecting diffusion-weighted images). T_1-weighted structural images for each participant at 0.75 mm^3 isotropic resolution were acquired to be used as a reference to segment corpus callosum. Diffusion-weighted data were acquired using a bipolar planar diffusion imaging pulse sequence: TE/TR = 86/5,900 ms, matrix size = 142 × 142, iPAT = 4, bandwidth = 1,136 Hz/pixel and 50 slices with an isotropic resolution of 1.5 mm × 1.5 mm × 1.5 mm. Gradient pulse duration = 26.82 ms and separation = 41.98 ms. Eleven *b*-values between 0 and 5,000 s/mm^2 in steps of 500 s/mm^2 were acquired. The number of gradient directions increased with *b*-value and set to maintain a consistent signal-to-noise ratio as a function of *b*-value, as specified in Table 1. We acquired two zero *b*-value images, and gradient strength was varied to achieve different *b*-values. Images were motion and eddy current corrected.

Table 1: The number of gradient directions acquired for each *b*-value in *in vivo* study. These were chosen to increase signal-to-noise ratio with increase in *b*-value.

b-value (s/mm^2)	500	1,000	1,500	2,000	2,500	3,000	3,500	4,000	4,500	5,000
Number of diffusion directions	3	3	6	6	9	12	15	18	21	24

2.6 Segmentation of the corpus callosum

Using MIPAV v7.1.1, we manually segmented the corpus callosum in the mid-sagittal plane in the trace image generated from the diffusion-weighted data. We used corresponding T_1-weighted images in each participant to aid the identification of the boundary of the corpus callosum. Adjacent slices were checked to minimise partial volume effects from other brain regions. The genu, mid-body and splenium were segmented separately.

3. Results

3.1 Fitting of the ActiveAx signal

Tables 2 and 3 provide the MRE and AICc for the diffusion models studied when axial diffusivity and diffusion time (Δ) were varied in the tissue model in the absence of noise. The MONO model performed worst. The BI model fitted the noiseless data best, and the anomalous diffusion models (STRETCHED, CTRW and FBTE) also achieved a very good fit to the data.

Table 2: The mean relative errors (%) of noiseless data fitting using the MONO, BI, STRETCHED, CTRW and FBTE models. We considered distinct and realistic diffusivities D_i = 0.6 µm^2/ms, D_{ii} = 1.0 µm^2/ms, D_{iii} = 1.4 µm^2/ms and D_{iv} = 1.8 µm^2/ms, and three diffusion time regimes, SHORT (Δ = 10 ms) with δ = 5 ms, MEDIUM (Δ = 50 ms) with δ = 10 ms and LONG (Δ = 100 ms) with δ = 20 ms, in the tissue model.

Diffusion time	Diffusivity	MONO	BI	STRETCHED	CTRW	FBTE
SHORT	0.6	13.04	0.93	1.93	0.29	1.93
	1.0	25.73	1.48	8.46	1.91	8.46
	1.4	38.21	1.35	15.56	5.75	15.56
	1.8	47.91	1.09	20.50	9.43	20.50
	mean	*31.22*	*1.21*	*11.61*	*4.35*	*11.61*
MEDIUM	0.6	8.35	0.53	1.79	0.37	1.79
	1.0	19.85	0.58	5.94	2.00	5.94
	1.4	31.35	0.55	9.52	4.46	9.52
	1.8	40.75	0.53	11.32	6.41	11.32
	mean	*25.08*	*0.55*	*7.14*	*3.31*	*7.14*
LONG	0.6	8.79	0.48	1.94	0.42	1.94
	1.0	20.20	0.47	5.81	2.55	5.81
	1.4	30.99	0.39	8.80	5.36	8.80
	1.8	39.69	0.31	10.26	7.32	10.26
	mean	*24.92*	*0.41*	*6.70*	*3.91*	*6.70*

Table 3: The corrected Akaike Information Criterion for the MONO, BI, STRETCHED, CTRW and FBTE models corresponding to Table 2.

Diffusion time	Diffusivity	MONO	BI	STRETCHED	CTRW	FBTE
SHORT	0.6	723.00	200.61	366.16	20.83	368.33
	1.0	759.27	211.13	543.83	330.00	546.00
	1.4	802.41	148.94	614.33	463.94	616.50
	1.8	833.49	76.81	644.16	524.37	646.33
	mean	*779.54*	*159.37*	*542.12*	*334.79*	*544.29*
MEDIUM	0.6	707.66	170.47	414.86	130.35	417.03
	1.0	811.52	124.27	584.38	435.80	586.55
	1.4	871.51	64.54	646.79	546.26	648.96
	1.8	908.02	25.12	668.38	591.97	670.55
	mean	*824.68*	*96.10*	*578.60*	*426.10*	*580.77*
LONG	0.6	733.42	177.17	445.18	168.67	447.35
	1.0	838.97	121.73	609.18	475.64	611.35
	1.4	898.22	45.31	668.08	583.72	670.25
	1.8	934.06	-29.09	687.25	627.27	689.42
	mean	*851.17*	*78.78*	*602.42*	*463.83*	*604.59*

The effect of axial diffusivity on goodness-of-fit was also evaluated. Table 2 shows that fitting errors generally increased as a function of axial diffusivity, except for the BI model.

3.2 Relationship between ActiveAx settings and diffusion model parameters

Figs. 3-7 provide the results for different models for different values of mean axon radius and axial diffusivity in the tissue model in the absence of noise. Results for the MONO model are shown in Fig. 3, for the BI model in Fig. 4 and for the STRETCHED model in Fig. 5. The parameter α differentiates the STRETCHED model from the MONO model. Results for the CTRW and FBTE anomalous diffusion models are provided in Figs. 6 and 7. Evaluation of r^2, m and c from linear regression analysis in Figs 3-7 indicates that the FBTE model yielded the best goodness-of-fit and reflected the value of D set in the tissue model. In addition, the FBTE model produced the most consistent value for D as a function of mean axon radius. D predicted using other models showed greater variation as a function of mean axon radius.

Figure 3: The simulation results of MONO model for different axial diffusivity of different Δ and δ, Δ = 10 ms and δ = 5 ms (column 1), Δ = 50 ms and δ = 10 ms (column 2) and Δ = 100 ms and δ = 20 ms (column 3) in the tissue model in the absence of noise. The unit of diffusivity D is $\mu m^2/ms$, and the unit of mean axon radius is μm and r^2 represents the association between the axial diffusivity set in ActiveAx and the diffusivity estimated using the model.

Figure 4: The simulation results of BI model for different axial diffusivity of different Δ and δ, Δ = 10 ms and δ = 5 ms (column 1), Δ = 50 ms and δ = 10 ms (column 2) and Δ = 100 ms and δ = 20 ms (column 3) in the tissue model in the absence of noise. The units of diffusivities D_1 and D_2 are $\mu m^2/ms$, and the unit of mean axon radius is μm and r^2 represents the association between the axial diffusivity set in ActiveAx and the diffusivity estimated using the model. V represents the volume fraction of the compartment at diffusivity D_1. Here, we only report regression results based on D_1, since D_2 produced worst results.

Figure 5: The simulation results of STRETCHED model for different axial diffusivity of different Δ and δ, Δ = 10 ms and δ = 5 ms (column 1), Δ = 50 ms and δ = 10 ms (column 2) and Δ = 100 ms and δ = 20 ms (column 3) in the tissue model in the absence of noise. The unit of diffusivity D is $\mu m^2/ms$, and the unit of mean axon radius is μm and r^2 represents the association between the axial diffusivity set in ActiveAx and the diffusivity estimated using the model.

Figure 6: The simulation results of CTRW model for different axial diffusivity of different Δ and δ, Δ = 10 ms and δ = 5 ms (column 1), Δ = 50 ms and δ = 10 ms (column 2) and Δ = 100 ms and δ = 20 ms (column 3) in the tissue model in the absence of noise. The unit of diffusivity D_m is $\mu m^2/ms$, and the unit of mean axon radius is μm and r^2 represents the association between the axial diffusivity set in ActiveAx and the diffusivity estimated using the model.

Figure 7: The simulation results of FBTE model for different axial diffusivity of different Δ and δ, Δ = 10 ms and δ = 5 ms (column 1), Δ = 50 ms and δ = 10 ms (column 2) and Δ = 100 ms and δ = 20 ms (column 3) in the tissue model in the absence of noise. The unit of diffusivity D is $\mu m^2/ms$, and the unit of mean axon radius is μm and r^2 represents the association between the axial diffusivity set in ActiveAx and the diffusivity estimated using the model.

Figs. 8 and 9 summarise the results of the sensitivity analysis for NORMAL and LOW SNRs levels of Rician noise. $\mathcal{E}$ represents the difference (%) between parameter estimates for noisy versus noiseless data. The dashed line in Fig. 8 represents a 1% level of error and in Fig. 9 it corresponds to 2% error. The BI model is more sensitive to noise than the other models. The MONO model is appears least sensitive to noise, closely followed by the STRETCHED and FBTE models.

Figure 8: The results of the sensitivity analysis when SNR = 15 dB (corresponding to a SNR = 30 computed in the standard way). Shown are the results of all models considered across four distinct axial diffusivities (D_i to D_{iv}) and three diffusion time regimes (SHORT, MEDIUM and LONG). The error bars correspond to one standard deviation from the mean computed based on repetitions of simulations. On the y-axis $\mathcal{E}$ represents the error (%) by which the parameter estimates varied with respect to the noiseless parameter estimate. For the purpose of interpretation we have included a dashed line corresponding to the 1% error level.

Figure 9: The results of the sensitivity analysis when SNR = 10 dB (corresponding to a SNR = 10 computed in the standard way). Shown are the results of all models considered across four distinct axial diffusivities (D_i to D_{iv}) and three diffusion time regimes (SHORT, MEDIUM and LONG). The error bars correspond to one standard deviation from the mean computed based on repetitions of simulations. On the y-axis $\mathcal{E}$ represents the error (%) by which the parameter estimates varied with respect to the noiseless parameter estimate. For the purpose of interpretation we have included a dashed line corresponding to the 2% error level.

3.3 **Assessment of diffusion model performance**

Parameters of the anomalous diffusion models were sensitive to changes in mean axon radius and axial diffusivity (Table 4). Of the five models considered, the FBTE model was most sensitive to changes in ActiveAx tissue parameters. Note, the SHORT diffusion time regime results should be interpreted carefully, since δ and Δ may not satisfy ActiveAx assumptions when mean axon radii become large.

Table 4: Summary of model performance based on the ability to provide information about ActiveAx tissue parameters using criteria A-D. The numbers of model parameters are in parentheses next to the model name. The results are calculated for all axon radii. The ranking value in criterion A means how well the diffusion coefficient in the model captures axial diffusivities set in ActiveAx. Here, a rank of 1 corresponds to the best fit. The percentages in criteria B-D mean the percentage of model parameters which meet the criteria of: (B) non-intersecting curves, (C) one-to-one mapping, and (D) wide ranging sensitivity to tissue microstructure characteristics. Note, we did not use μ in the FBTE model in this classification as it is only a unit preserving parameter. The best performing model for each criterion has been highlighted. Light grey to the model which perform better in each criterion in each diffusion time regime, and darker grey to the best overall model when multiple models performed equally well.

Criterion	Short diffusion time Δ = 10 ms, δ = 5 ms	Medium diffusion time Δ = 50 ms, δ = 10 ms	Long diffusion time Δ = 100 ms, δ = 20 ms

Model	A *rank*	B *%*	C *%*	D *%*	A *rank*	B *%*	C *%*	D *%*	A *rank*	B *%*	C *%*	D *%*
MONO (1)	4	100	-	0	5	100	-	0	5	100	-	0
BI (3)	5	0	0	0	3	0	0	0	3	67	50	0
STRETCHED (2)	3	50	0	50	4	100	100	100	4	100	100	100
CTRW (3)	2	33	0	33	2	33	0	33	2	33	0	33
FBTE (3)	1	50	0	50	1	100	100	100	1	100	100	100

3.4 *In vivo* results

Fig. 10 provides the corpus callosum results for the FBTE model parameters evaluated from the *in vivo* MRI data. The top three plots show how D, β and μ from the FBTE model behave as a function of mean axon radius when ActiveAx is used to simulate the signals based on the *in vivo* gradient pulse duration and diffusion times. These plots are comparable to parameter trends in Fig. 7. The mean squared errors between calculated diffusivity D and axial diffusivities (D_{i} = 0.6 μm^2/ms, D_{ii} = 1.0 μm^2/ms, D_{iii} = 1.4 μm^2/ms and D_{iv} = 1.8 μm^2/ms) set in ActiveAx are 0.0038%, 0.06%, 0.68% and 1.00%, respectively, and the corresponding maximum relative errors are 1.33%, 4.80%, 11.86% and 9.94%.

The rest of Fig. 10 shows the spatially resolved maps of D, β and μ in the corpus callosum for the five participants. All five participants (P1 to P5) have very similar diffusion coefficients (P1: D = 1.00 ± 0.03 μm^2/ms; P2: D = 1.03 ± 0.05 μm^2/ms; P3: D = 1.01 ± 0.03 μm^2/ms; P4: D = 1.02 ± 0.04 μm^2/ms; P5: D = 1.00 ± 0.02 μm^2/ms), none of which differed significantly ($p > 0.05$). The β values in the corpus callosum for five participants were 0.64 ± 0.08 (P1), 0.54 ± 0.09 (P2), 0.63 ± 0.10 (P3), 0.58 ± 0.05 (P4) and 0.62 ± 0.07 (P5). Based on the simulated trend in β as a function of mean axon radius, and by noting that D_{ii} is mostly 1.0 μm^2/ms, the spatial variation in mean axon radius can directly be inferred from the trend in β.

Figure 10: FBTE model results obtained using the *in vivo* MRI data in the corpus callosum of five participants (P1 to P5). The top three plots illustrate simulation results based on diffusion times from the *in vivo* experiment (Δ = 41.98 ms and δ = 26.82 ms). Mean axon radius is measured in µm and r^2 represents the association between the axial diffusivity set in ActiveAx and the diffusivity estimated using the model. The rest of the figure shows spatially resolved maps of D (in μm^2/ms), β and μ. Locations (i)-(iii) correspond to the genu, mid-body and splenium regions of the corpus callosum.

Table 4 shows that the STRETECHED model, apart from criteria A, performs as well as FBTE. Fig. 11 provides the *in vivo* findings using the STRETCHED model. The mean squared errors between calculated diffusivity D and axial diffusivities (D_{i} = 0.6 μm^2/ms, D_{ii} = 1.0 μm^2/ms, D_{iii} = 1.4 μm^2/ms and D_{iv} = 1.8 μm^2/ms) set in ActiveAx were 4.5%, 17.98%, 42.15% and 75.34%, and the corresponding maximum relative errors were 52.67%, 58.10%, 61.00% and 61.89%. Fig. 11 also shows the spatially resolved maps of D and α in the corpus callosum for the five participants. All five participants (P1 to P5) have very different diffusion coefficients with large standard deviations (P1: D = 0.67 ± 0.22

μm^2/ms; P2: D = 0.97 ± 0.35 μm^2/ms; P3: D = 0.93 ± 0.39μm^2/ms; P4: D = 0.70 ± 0.23 μm^2/ms; P5: D = 0.78 ± 0.20 μm^2/ms). The α values in the corpus callosum for five participants were 0.64 ± 0.08 (P1), 0.54 ± 0.09 (P2), 0.65 ± 0.12 (P3), 0.58 ± 0.05 (P4) and 0.62 ± 0.07 (P5), that correspond to the β values from Fig. 10 with the exception of P3.

Figure 11: STRETCHED model results obtained using the *in vivo* MRI data in the corpus callosum of five participants (P1 to P5). The top two plots illustrate simulation results based on diffusion times from the *in vivo* experiment (Δ = 41.98 ms and δ = 26.82 ms). Mean axon radius is measured in µm and r^2 represents the association between the axial diffusivity set in ActiveAx and the diffusivity estimated using the model. The rest of the figure shows spatially resolved maps of D (in μm^2/ms) and α. Locations (i)-(iii) correspond to the genu, mid-body and splenium regions of the corpus callosum.

4. Discussion

We investigated how diffusion model parameters vary as a function of mean axon radius to define the best model for mean axon radius estimation. Whilst we found the bi-exponential model fitted noiseless data best, the model performed worst in the presence of noise. All of the anomalous diffusion models (STRETCHED, CTRW and FBTE) were less noise sensitive than the bi-exponential model (Figs. 8 and 9). Using a number model selection criteria (summarised in Table 4), we demonstrated that the FBTE model parameters were able to reflect changes in mean axon radius. We were also able to resolve variations in model parameters in the corpus callosum in five healthy participants, suggesting that changes in mean axon radius can be inferred from model parameters. To our knowledge, this is the first systematic evaluation of the utility of anomalous diffusion models in evaluating changes in white matter microstructure. Whilst we investigated the relationship between various anomalous diffusion model parameters and ActiveAx tissue model settings, and ranked models in terms of our criteria, different models may provide different types of information in other applications. For example, anomalous diffusion has been proposed for the study of sub-diffusion, cellular order and disorder (Palombo et al. 2011, 2013). It is likely that different anomalous diffusion models have distinct pros and cons depending on the application studied.

4.1 *In vivo* findings

In vivo MRI findings showed that the diffusion coefficient D in the FBTE model did not differ greatly between different parts of the corpus callosum in the mid-sagittal plane or between participants (Fig. 10). The mapped value of D was also able to capture the axial diffusivity set in ActiveAx and did not change greatly with changes in mean axon radius. *In vivo* findings resembled the high-low-high distribution in D along the corpus callosum demonstrated previously (Rimkus et al., 2013). Notably, based on our simulation findings, D estimated using the FBTE model reflects axial diffusivity set in ActiveAx. $\mathbf{D}_{\text{eff}}$, derived from axial diffusivity ($D_{/\!/}$) and apparent diffusivity ($D_{\perp}$) in ActiveAx, can be converted to a mean diffusivity by averaging the diagonal entries. Thus, axial and apparent diffusivities can be converted to a mean diffusivity. For a value of D = 1.00 μm^2/ms, which is representative of our *in vivo* findings, the mean diffusivity calculated from $\mathbf{D}_{\text{eff}}$ is 0.85 μm^2/ms. This value is in very close agreement with the mean diffusivity of 0.81 μm^2/ms in the corpus callosum

reported by Rimkus et al. (2013), and 0.86 $\mu m^2/ms$ found by Ibrahim et al. (2011). We found β from the FBTE model increased monotonically with mean axon radius, which means that for a fixed value of D, the mean axon radius can directly be inferred from β. It has previously been shown that the mean axon radius varies in the corpus callosum and exhibits a low-high-low trend going from the anterior (genu indicated by (i) in Fig. 10) to the middle (mid-body indicated as (ii) in Fig. 10) and posterior (splenium indicated by (iii) in Fig. 10) callosum (Caminiti et al., 2013; Yu et al., 2017). The expected low-high-low pattern is also present in maps of β. Additionally, Fig. 11 illustrates that D in the STRETCHED model did differ significantly between different parts of the corpus callosum and between participants, meaning that the STRETCHED model may not suitably capture information on diffusivity.

While other studies have examined fibre microstructure using diffusion-weighted images, none have assessed the appropriateness of the model used to inferring tissue properties. The CHARMED model (restricted and hindered diffusion signal compartments) was used to characterise anisotropic water diffusion in the pig spinal cord (Assaf et al., 2004). The model later evolved into the AxCaliber model, in which the fixed axon diameter distribution used in the CHARMED model was replaced by an axon diameter distribution computed from histology results (Assaf et al., 2008). Barazany et al. (2009) went on to incorporate an isotropic diffusion compartment into AxCaliber, which was used to account for partial volume effects from CSF. They applied this three-compartment (hindered, restricted and isotropic diffusion) model to estimate the axon diameter distribution in the rat corpus callosum. Recently, NODDI, a three-compartment model incorporating intra-cellular, extra-cellular and CSF diffusion signal compartments was used to estimate the microstructural complexity of dendrites and axons (Zhang et al., 2012). The NODDI model was able to provide *in vivo* estimates of neurite density and orientation dispersion. Our approach is unique in being a systematic evaluation of the models, allowing us to identify the model (i.e. FBTE) best suited for characterising white matter. Our heuristic could be applied to future studies investigating the role of model selection for other quantitative diffusion imaging applications.

4.2 Relationship between ActiveAx settings and diffusion model parameters

The STRETCHED, CTRW and FBTE models were found to be more sensitive to ActiveAx tissue parameters than the MONO and BI models based on our criteria, summarised in Table 4. Individual model parameters of each diffusion model cannot be compared directly and have been assigned different meanings in the literature based on how the equations were derived. Parameter α in the STRETCHED model and β in the FBTE model were similar for the three diffusion time regimes studied (compare Figs. 5 and 7). Parameters α and β in the CTRW model and μ in the FBTE model were affected differently by changes in mean axon radius and axial diffusivity (compare Figs. 6 and 7). These findings imply that the anomalous diffusion equations share some characteristics but that different parameters also capture different information about tissue parameters. Hence, it would be interesting to study how parameters of the different models behave under different microstructural situations.

4.3 Existing findings using anomalous diffusion models

Our findings showed that parameter α in the STRETCHED model is sensitive to changes in tissue microstructure, as has been shown previously (Bai et al., 2016). Parameter α was suggested to correlate with tissue heterogeneity where a lower value indicates a more heterogeneous microstructure (Bennett et al., 2003).

In a short diffusion time study using a fixed rat brain, the information in maps of α and β from the CTRW model were stated to reflect tissue porosity and tortuosity (Magin et al., 2013). Specifically, a smaller α corresponded to lower porosity and a smaller β corresponded to lower tortuosity. We found α to be smaller for smaller mean axon radii, corresponding to denser packing and lower porosity. Parameter β showed a tendency to decrease for smaller mean axon radii, which also confirms the findings in fixed rat brain relating to tissue tortuosity. In addition, we found parameter β was more sensitive to changes in axial diffusivity than parameter α. Karaman et al. (2016a) has also found that parameter β from the CTRW model can be used to classify tissue.

Our findings show that parameter β in the FBTE model correlates well with tissue parameters, as previously observed in a study of healthy brains (Zhou et al., 2010). Parameter β was suggested to correlate with tissue heterogeneity with a smaller β reflecting greater tissue heterogeneity. Others have also found the parameters of the FBTE model to correlate with tissue heterogeneity (Sui et al., 2015, 2016). Our approach of connecting anomalous diffusion parameters from the FBTE model to tissue microstructure may provide insight into neurodegenerative diseases and disorders wherein tissue microstructural reorganization occurs. It may also aid the development of biomarkers for the purpose of disease detection and longitudinal monitoring of changes in tissue.

4.4 Other fractional diffusion models

Our work focused on investigating models which can be applied to data readily acquired using human MRI scanners. Other anomalous diffusion models have been developed to date, including time and space-time fractional forms. The different types of models are applicable to different types of data. Notably, time and space-time fractional models generally require data in which both the diffusion time and gradient strength change. To obtain multiple diffusion time data, the sequence has to be repeated with a new diffusion time setting. This leads to repeated diffusion weighted image acquisitions, which in turn lead to prolonged scan times. In fact, these scan times become implausible for routine use on scanners available today. Nevertheless, it would be interesting to investigate the use of time and space-time fractional models in a study similar to this one.

Magin et al. (2008) developed three models, the space fractional model used herein, and a time and a space-time fractional model. The latter two have specific shortcomings, as they cannot be used with the short gradient pulse approximation and thereby theoretical limitations have been identified (Lin 2015). Recently, a modified-Bloch equation for anomalous diffusion (space-time fractional) was proposed by Lin (2017a, 2017b) in view of limitations associated with the short gradient pulse approximation. In addition, based on the space-time fractional diffusion equation used by Magin et al. (2008), Lin (2016) developed the effective phase diffusion equation method and the non-Gaussian

approximation method. Both temporal and spatial fractional parameters were determined in the presence of small signal attenuation (Lin 2016), which could be useful in the future studies which involve multiple diffusion time data.

Eliazar and Shlesinger (2013) originally introduced the general theory of fractional motion (FM) in relation to macroscopic effects due to microscopic level details. Fan and Gao (2015) extended the FM theory to DW-MRI to be able to describe signal influences in terms of the statistical properties of water diffusion in tissue. Their FM model parameter maps showed exquisite soft tissue contrast. However, the FM model requires data wherein both the gradient strength and diffusion time change (i.e. fractional in time). Later, the FM model was shown to have similar characteristics to those of the CTRW model, wherein gradient strength and not diffusion time was changed to change the b-value (Karaman et al., 2016b).

4.5 Limitations

A recent work by Caporale et al. (2017) highlighted that local magnetic susceptibility differences, which influence MRI signal formation, likely affect model parameters. This was concluded in view of studying white matter influences on model parameters in (12). They established that parameter 2μ in (12) mapped in the human brain, which is named $\gamma=2\mu$ in Caporale et al. (2017), depends on local magnetic susceptibility differences between myelin and extracellular space (Caporale et al., 2017). We did not account for magnetic susceptibility influences in our models. Therefore, we might have underestimated the sensitivity of anomalous diffusion CTRW parameters to white matter tissue parameters.

In this study, we did not acquired diffusion-weighted low *b*-value data, such as in the range 0 to 500 s/mm^2, which may additionally improve the quantification of anomalous diffusion model parameters. The tissue model we used assumed no water molecule exchange occurs between compartments, which may not be the case in general in the brain. Additionally, the tissue model only considered axonal structures and assumed a single axon orientation within the voxel. Crossing, bending or fanning fibres in white matter could be considered in a future study.

5. Conclusions

We evaluated the sensitivity of anomalous diffusion models to white matter tissue parameters using ActiveAx, a white matter tissue model proposed by Alexander et al. (2010). Our work demonstrates that the choice of the diffusion model has a significant impact on the ability to infer information about white matter microstructure from diffusion weighted MRI data. Our results suggest that classical models do not perform as well as anomalous diffusion models in the presence of noise. In particular, the space fractional Bloch-Torrey model appears to be the best candidate to axonal properties.

Acknowledgments

Dr Qiang Yu acknowledges the University of Queensland for the award of a UQ Postdoctoral Research Fellowship (No. 2013002003) for financial support. Professor David Reutens and Dr Viktor Vegh acknowledge the Australian Research

Council for the award of a Discovery Project Grant (DP140103593). We also wish to thank the three expert reviewers who provided feedback on our manuscript.

References

[1] Abragam A. Principles of nuclear magnetism. Oxford: Oxford University Press; 2011.

[2] Alexander DC, Hubbard PL, Hall MG, Moore EA, Ptito M, Parker GJM, et al. Orientationally invariant indices of axon diameter and density from diffusion MRI. Neuroimage. 2010; 52: 1374-1389.

[3] Anderson DR, Burnham KP, White GC. AIC model selection in overdispersed capture-recapture data. Ecology. 1994; 75(6): 1780-1793.

[4] Assaf Y, Blumenfeld-Katzir T, Yovel Y, Basser PJ. AxCaliber: a method for measuring axon diameter distribution from diffusion MRI. Magn Reson Med. 2008; 59(6): 1347-1354.

[5] Assaf Y, Freidlin RZ, Rohde GK, Basser PJ. New modeling and experimental framework to characterize hindered and restricted water diffusion in brain white matter. Magn Reson Med. 2004; 52: 965-978.

[6] Bai Y, Lin Y, Tian J, Shi D, Cheng J, Haacke EM, Hong X, Ma B, Zhou J, Wang M. Grading of gliomas by using monoexponential, biexponential, and stretched exponential diffusion-weighted MR imaging and diffusion kurtosis MR imaging. Radiology. 2016; 278(2): 496-504.

[7] Barazany D, Basser PJ, Assaf Y. In-vivo measurement of the axon diameter distribution in the corpus callosum of a rat brain. Brain. 2009; 132: 1210-1220.

[8] Basser PJ, Matiello J, LeBihan D. MR diffusion tensor spectroscopy and Imaging. Biophys J. 1994; 66: 259-267.

[9] Bennett KM, Schmainda KM, Rowe DB, Lu H, Hyde JS. Characterization of continuously distributed cortical water diffusion rates with a stretched-exponential model. Magn Reson Med. 2003; 50(4): 727-734.

[10] Bhalekar S, Daftardar-Gejji V, Baleanu D, and Magin R. Fractional Bloch equation with delay. Comput Math Appl. 2011; 61(5): 1355-1365.

[11] Caminiti R, Carducci F, Piervincenzi C, Battaglia-Mayer A, Confalone G, Visco-Comandini F, Pantano P, Innocenti GM. Diameter, length, speed, and conduction delay of callosal axons in macaque monkeys and humans: comparing data from histology and magnetic resonance imaging diffusion tractography. J Neurosci. 2013; 33(36): 14501-14511.

[12] Caporale A, Palombo M, Macaluso E, Guerreri M, Bozzali M, Capuani S. The γ-parameter of anomalous diffusion quantified in human brain by MRI depends on local magnetic susceptibility differences. Neuroimage. 2017; 147: 619-631.

[13] Capuani S, Palombo M, Gabrielli A, Orlandi A, Maraviglia B, Pastore FS. Spatio-temporal anomalous diffusion imaging: results in controlled phantoms and in excised human meningiomas. Magn. Reson. Imaging. 2013; 31(3): 359-365.

[14] Clark CA, Le Bihan D. Water diffusion compartmentation and anisotropy at high b values in the human brain. Magn Reson Med. 2000; 44(6): 852-859.

[15] De Santis S, Gabrielli A, Bozzali M, Maraviglia B, Macaluso E, Capuani S. Anisotropic anomalous diffusion assessed in the human brain by scalar invariant indices. Magn Reson Med. 2011; 65(4): 1043-1052.

[16] Eliazar II, Shlesinger MF. Fractional motions. Phys Rep. 2013; 527(2): 101-129.

[17] Fan Y, Gao JH. Fractional motion model for characterization of anomalous diffusion from NMR signals. Phys Rev E. 2015; 92(1): 012707.

[18] Gao Q, Srinivasan G, Magin R, Zhou X. Anomalous diffusion measured by a twice-refocused spin echo pulse sequence: analysis using fractional order calculus. J Magn Reson Imaging. 2011; 33: 1177-1183.

[19] Hansen DF, and Led JJ. Implications of using approximate Bloch–McConnell equations in NMR analyses of chemically exchanging systems: application to the electron self-exchange of plastocyanin. J Magn Reson. 2003; 163(2): 215-227.

[20] Hilfer R. Applications of fractional calculus in physics. World Scientific Publishing: New York; 2000.

[21] Hosking JR. Modeling persistence in hydrological time series using fractional differencing. Water Resour Res. 1984; 20(12): 1898-1908.

[22] Ibrahim I, Tintera J, Skoch A, Jirů F, Hlustik P, Martinkova P, Zvara K, Rasova K. Fractional anisotropy and mean diffusivity in the corpus callosum of patients with multiple sclerosis: the effect of physiotherapy. Neuroradiology. 2011; 53(11): 917-926.

[23] Ingo C, Sui Y, Chen Y, Parrish TB, Webb AG, Ronen I. Parsimonious continuous time random walk models and kurtosis for diffusion in magnetic resonance of biological tissue. Front Phys. 2015; 3: 11.

[24] Karaman MM, Sui Y, Wang H, Magin RL, Li Y, and Zhou XJ. Differentiating low- and high-grade pediatric brain tumors using a continuous-time random-walk diffusion model at high b-values. Magn Reson Med. 2016a; 76: 1149–1157.

[25] Karaman MM, Wang H, Sui Y, Engelhard HH, Li Y, Zhou XJ. A fractional motion diffusion model for grading pediatric brain tumors. NeuroImage: Clinical. 2016b; 12: 707-714.

[26] Kilbas AA, Srivastava HM, Trujillo JJ. Theory and applications of fractional differential equations. 1st ed. Amsterdam: Elsevier; 2006.

[27] Kimmich R. Strange kinetics, porous media, and NMR. Chem Phys. 2002; 284(1): 253-285.

[28] Köpf M, Metzler R, Haferkamp O, Nonnenmacher TF. NMR studies of anomalous diffusion in biological tissues: experimental observation of Lévy stable processes. In: Fractals in Biology and Medicine. Birkhäuser Basel: Springer; 1998. pp. 354-364.

[29] Le Bihan D. The ‘wet mind’ water and functional neuroimaging. Phys Med Biol. 2007; 52(7): R57-R90.

[30] Lin G. An effective phase shift diffusion equation method for analysis of PFG normal and fractional diffusions. J. Magn. Reson. 2015: 259: 232-240.

[31] Lin G. Analyzing signal attenuation in PFG anomalous diffusion via a non-gaussian phase distribution approximation approach by fractional derivatives. J. Chem. Phys. 2016: 145(19): 194202.

[32] Lin G. Fractional differential and fractional integral modified-Bloch equations for PFG anomalous diffusion and their general solutions. arXiv preprint arXiv:1702.07116. 2017a.

[33] Lin G. The exact PFG signal attenuation expression based on a fractional integral modified-Bloch equation. arXiv preprint arXiv:1706.02026. 2017b.

[34] Magin R, Abdullah O, Baleanu D, Zhou X. Anomalous diffusion expressed through fractional order differential operators in the Bloch-Torrey equation. J Magn Reson. 2008; 190(2): 255-270.

[35] Magin R, Feng X, Baleanu D. Solving the fractional order Bloch equation. Concepts Magn Reson Part A Bridg Educ Res. 2009; 34A(1): 16-23.

[36] Magin RL, Ingo C, Colon-Perez L, Triplett W, Mareci TH. Characterization of anomalous diffusion in porous biological tissues using fractional order derivatives and entropy. Microporous Mesoporous Mater. 2013; 178: 39-43.

[37] Novikov DS, Jespersen SN, Kiselev VG, Fieremans E. Quantifying brain microstructure with diffusion MRI: Theory and parameter estimation. arXiv preprint arXiv:1612.02059. 2016.

[38] Metzler R, and Klafter J. The random walks guide to anomalous diffusion: A fractional dynamics approach. Phys Rep. 2000; 339: 1-77.

[39] Mori S, Zhang J. Principles of diffusion tensor imaging and its applications to basic neuroscience research. Neuron. 2006; 51(5): 527-539.

[40] Palombo M, Gabrielli A, De Santis S, Cametti C, Ruocco G, Capuani S. Spatio-temporal anomalous diffusion in heterogeneous media by nuclear magnetic resonance. J. Chem. Phys. 2011; 135(3): 034504.

[41] Palombo M, Gabrielli A, De Santis S, Capuani S. The γ parameter of the stretched-exponential model is influenced by internal gradients: validation in phantoms. J. Magn. Reson. 2012; 216: 28-36.

[42] Palombo M, Gabrielli A, Servedio VD, Ruocco G, Capuani S. Structural disorder and anomalous diffusion in random packing of spheres. Sci. Rep. 2013; 3.

[43] Petráš I. Modeling and numerical analysis of fractional-order Bloch equations. Comput Math Appl. 2011; 61(2): 341-356.

[44] Price WS. NMR studies of translational motion: principles and applications. New York: Cambridge University Press; 2009.

[45] Pu Y, Zhou J, Yuan X. Fractional differential mask: a fractional differential-based approach for multiscale texture enhancement. IEEE Trans Image Process. 2010; 19(2): 491-511.

[46] Qin S, Liu F, Turner IW, Vegh V, Yu Q, Yang Q. Multi-term time-fractional Bloch equations and application in magnetic resonance imaging. J Comput Appl Math. 2017a; 319: 308-319.

[47] Qin S, Liu F, Turner IW, Yu Q, Yang Q, Vegh V. Characterization of anomalous relaxation using the time-fractional Bloch equation and multiple echo T2*-weighted magnetic resonance imaging at 7T. Magn Reson Med. 2017b; 77(4): 1485-1494.

[48] Rimkus CD, Junqueira TD, Callegaro D, Otaduy MC, Leite CD. Segmented corpus callosum diffusivity correlates with the Expanded Disability Status Scale score in the early stages of relapsing-remitting multiple sclerosis. Clinics. 2013; 68(8): 1115-1120.

[49] Scalas E, Gorenflo R, & Mainardi F. Fractional calculus and continuous-time finance. Physica A. 2000; 284(1): 376-384.

[50] Sen PN. Time-dependent diffusion coefficient as a probe of the permeability of the pore wall. J Chem Phys. 2003; 119(18): 9871-9876.

[51] Song J, Yu Q, Liu F, Turner I. A spatially second-order accurate implicit numerical method for the space and time fractional Bloch-Torrey equation. Numer Algorithms. 2014; 66(4): 911-932.

[52] Sui Y, Wang H, Liu G, Damen FW, Wanamaker C, Li Y, et al. Differentiation of low-and high-grade pediatric brain tumors with high b-value diffusion-weighted MR imaging and a fractional order calculus model. Radiology. 2015; 277(2): 489-496.

[53] Sui Y, Xiong Y, Jiang J, Karaman MM, Xie KL, Zhu W, Zhou XJ. Differentiation of low-and high-grade gliomas using high b-value diffusion imaging with a non-Gaussian diffusion model. AJNR Am J Neuroradiol. 2016. doi: 10.3174/ajnr.A4836

[54] Sun SW, Liang HF, Le TQ, Armstrong RC, Cross AH, & Song SK. Differential sensitivity of in vivo and ex vivo diffusion tensor imaging to evolving optic nerve injury in mice with retinal ischemia. Neuroimage. 2006a; 32(3): 1195-1204.

[55] Sun SW, Liang HF, Trinkaus K, Cross AH, Armstrong RC, & Song SK. Noninvasive detection of cuprizone induced axonal damage and demyelination in the mouse corpus callosum. Magn Reson Med. 2006b; 55(2): 302-308.

[56] Szafer A, Zhong J, Gore JC. Theoretical model for water diffusion in tissues. Magn Reson Med. 1995; 33(5): 697-712.

[57] Torrey HC. Bloch equations with diffusion terms. Phys Rev. 1956; 104(3): 563-565.

[58] Upadhyaya A, Rieu JP, Glazier JA, Sawada Y. Anomalous diffusion and non-Gaussian velocity distribution of Hydra cells in cellular aggregates. Physica A. 2001; 293(3): 549-558.

[59] van Gelderen P, Despres D, Vanzijl, PCM, Moonen CTW. Evaluation of restricted diffusion in cylinders. Phosphocreatine in rabbit leg muscle. J Magn Reson Ser B. 1994; 103(3): 255-260.

[60] Xu B, Gong G, Fan Y, Wu B, Gao JH. Directional sensitivity of anomalous diffusion in human brain assessed by tensorial fractional motion model. Magn Reson Imaging. 2017a; 42: 74-81.

[61] Xu B, Su L, Wang Z, Fan Y, Gong G, Zhu W, Gao P, Gao JH. Anomalous diffusion in cerebral glioma assessed using a fractional motion model. Magn Reson Med. 2017b; 78(5): 1944-1949.

[62] Yablonskiy DA, Sukstanskii AL. Theoretical models of the diffusion weighted MR signal. NMR Biomed. 2010; 23: 661-681.

[63] Yu Q, Liu F, Anh V, Turner I. Solving linear and nonlinear space-time fractional reaction-diffusion equations by Adomian decomposition method. Internat J Numer Meth Eng. 2008; 74: 138-158.

[64] Yu Q, Liu F, Turner I, Burrage K. A computationally effective alternating direction method for the space and time fractional Bloch-Torrey equation in 3-D. Appl Math Comput. 2012; 219: 4082-4095.

[65] Yu Q, Liu F, Turner I, Burrage K. Numerical investigation of three types of space and time fractional Bloch-Torrey equations in 2D. Cent Eur J Phys. 2013a; 11(6): 646-665.

[66] Yu Q, Liu F, Turner I, Burrage K. Stability and convergence of an implicit numerical method for the space and time fractional Bloch-Torrey equation. Phil Trans R Soc A. 2013b; 371(1990): 20120150. DOI: 10.1098/rsta.2012.0150

[67] Yu Q, Reutens D, O'Brien K, Vegh V. Tissue microstructure features derived from anomalous diffusion measurements in magnetic resonance imaging. Hum Brain Mapp. 2017; 38(2): 1068-1081.

[68] Yu Q, Vegh V, Liu F, & Turner I. A Variable Order Fractional Differential-Based Texture Enhancement Algorithm with Application in Medical Imaging. PloS one. 2015; 10(7): e0132952.

[69] Zaslavsky G. Chaos, fractional kinetics, & anomalous transport. Phys Rep. 2002; 371(6): 461-580.

[70] Zhang H, Schneider T, Wheeler-Kingshott CA, Alexander DC. NODDI: practical in vivo neurite orientation dispersion and density imaging of the human brain. Neuroimage. 2012; 61(4): 1000-1016.

[71] Zhou X, Gao Q, Abdullah O, Magin R. Studies of anomalous diffusion in the human brain using fractional order calculus. Magn Reson Med. 2010; 63(3): 562-569.

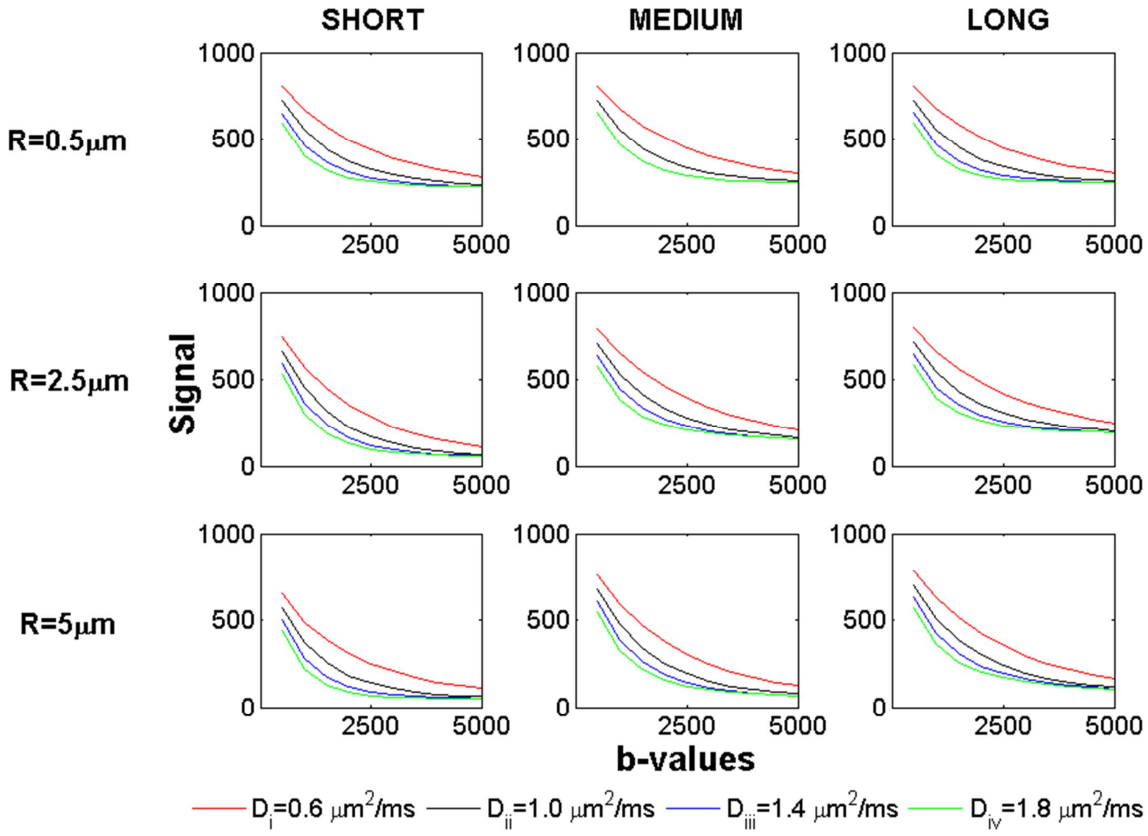

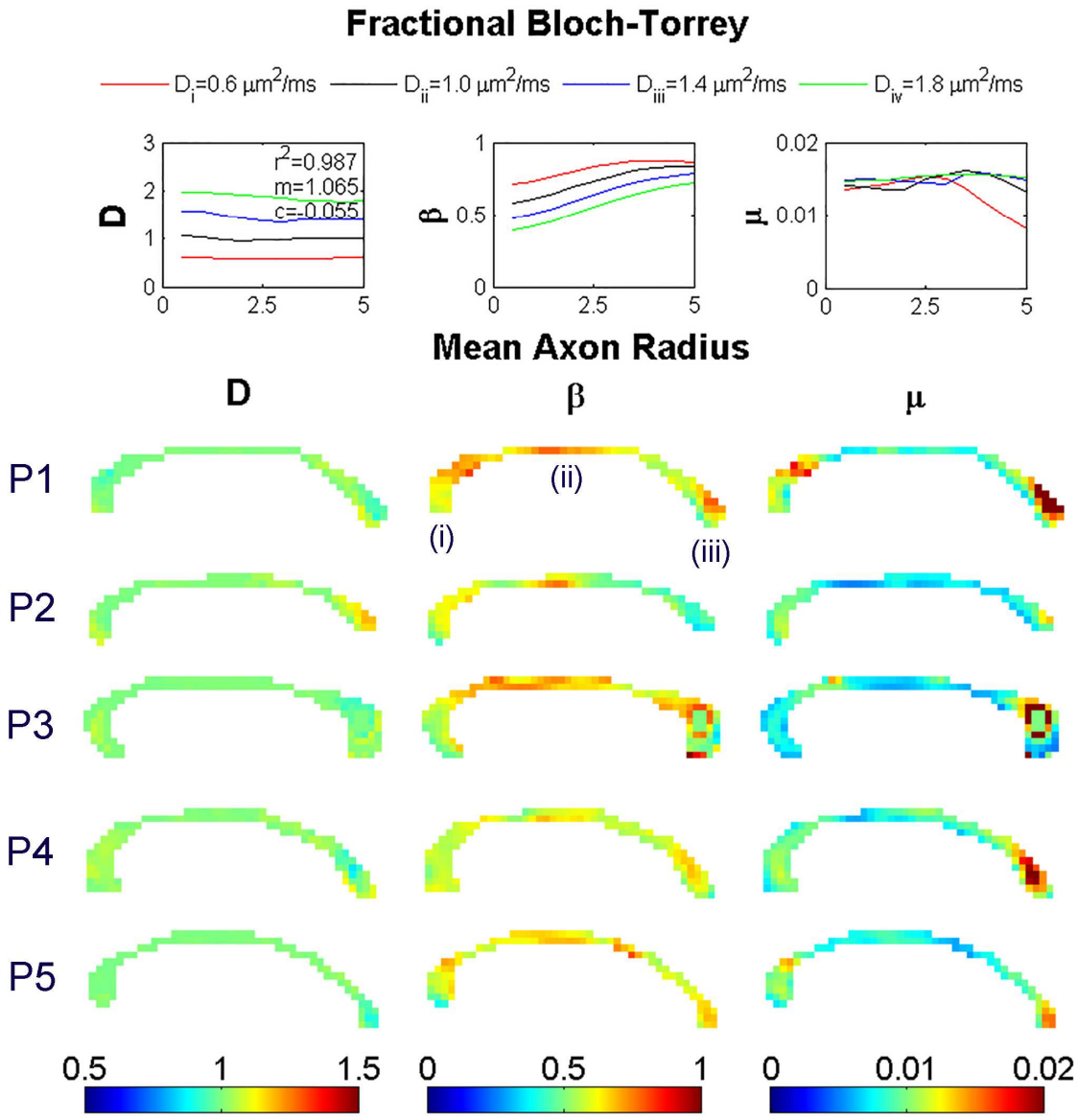
Fractional Bloch-Torrey
D_i=0.6 μm²/ms
D_ii=1.0 μm²/ms
D_iii=1.4 μm²/ms
D_iv=1.8 μm²/ms
D
r²=0.987
m=1.065
c=-0.055
β
μ
Mean Axon Radius
D
β
μ
P1
P2
P3
P4
P5
(i)
(ii)
(iii)
0.5 1 1.5
0 0.5 1
0 0.01 0.02

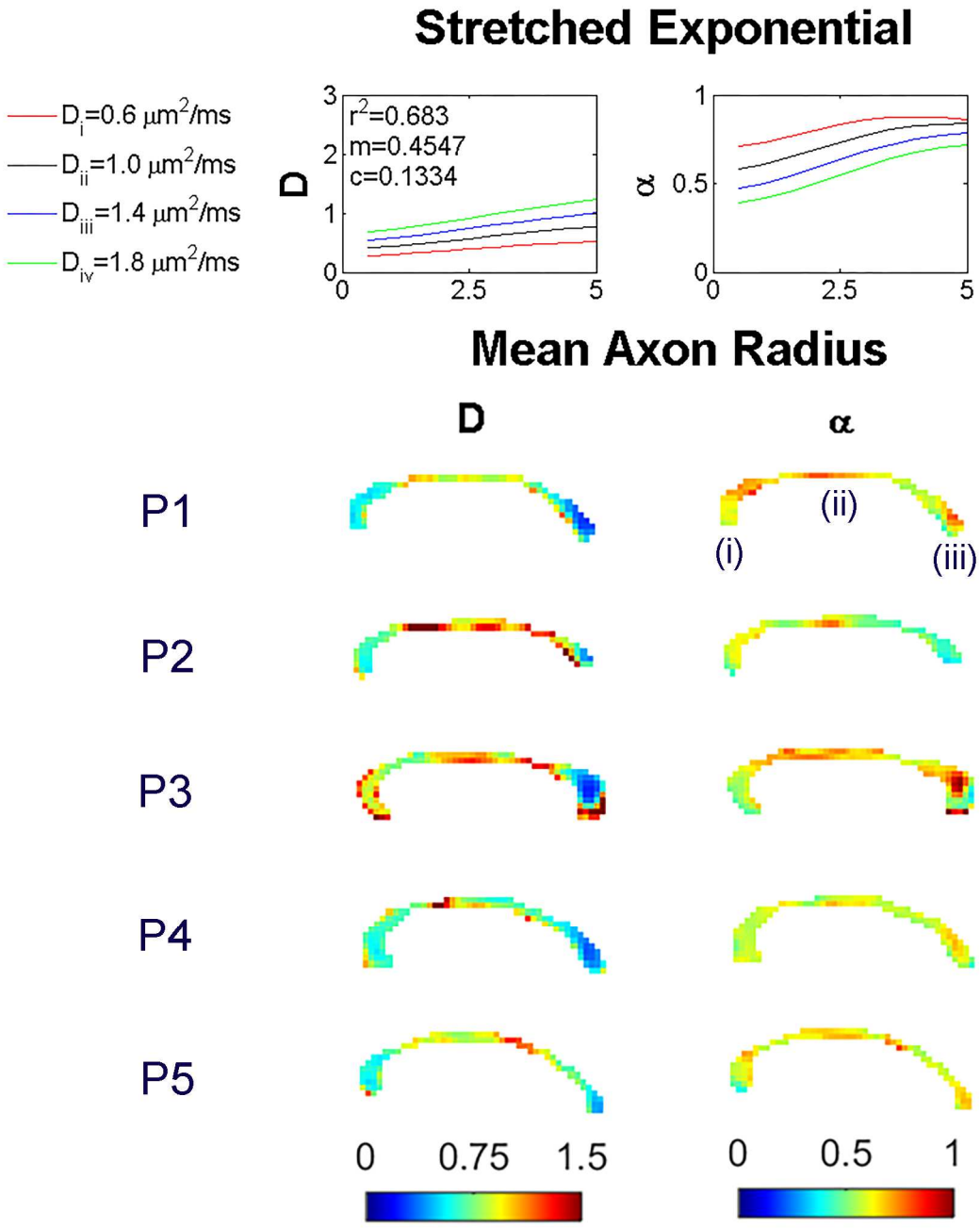
Stretched Exponential
D_i=0.6 μm²/ms
D_{ii}=1.0 μm²/ms
D_{iii}=1.4 μm²/ms
D_{iv}=1.8 μm²/ms
D
r²=0.683
m=0.4547
c=0.1334
α
Mean Axon Radius
D
α
P1
P2
P3
P4
P5
(i)
(ii)
(iii)
0 0.75 1.5
0 0.5 1

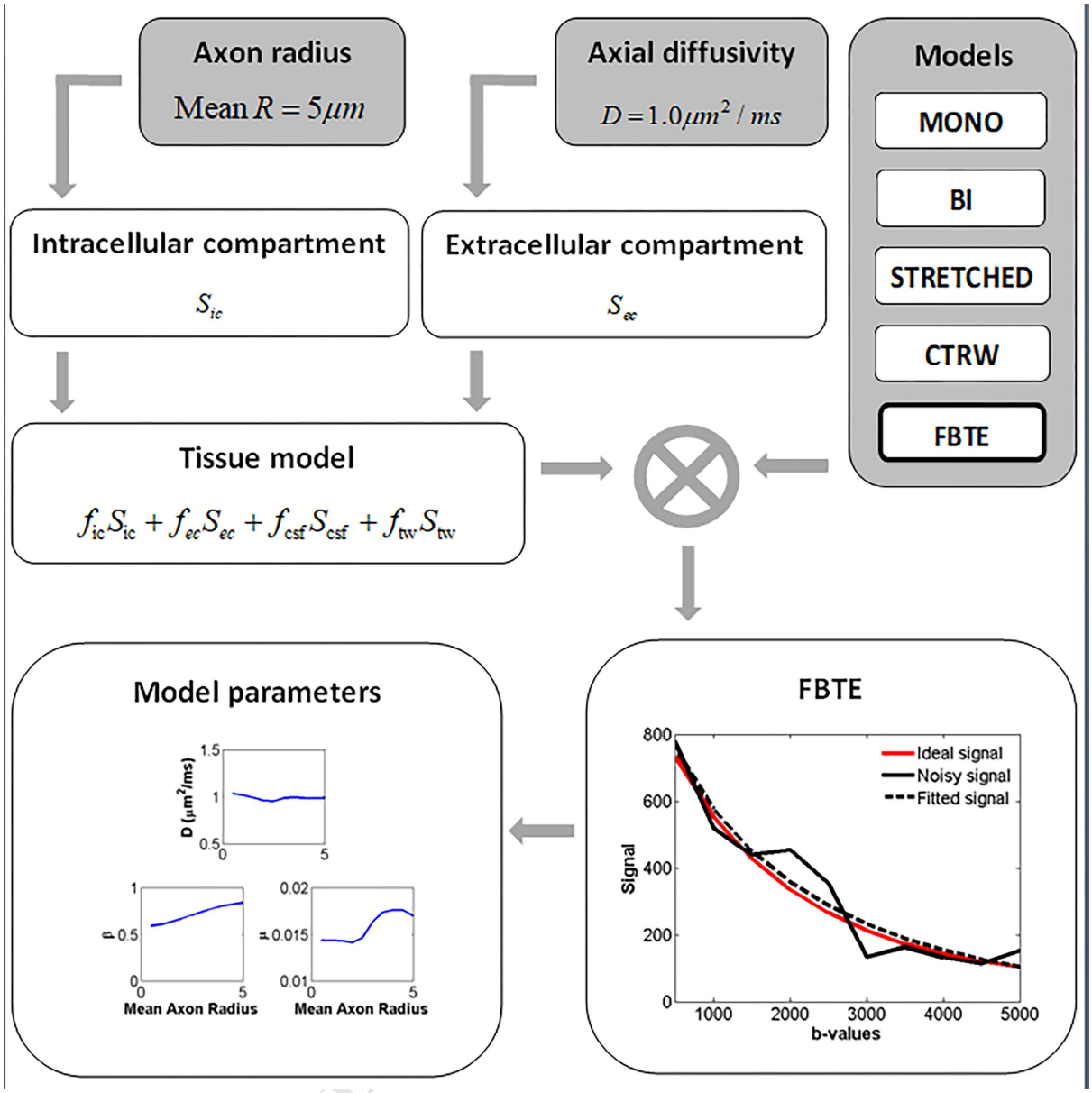
Axon radius
Mean $R = 5\mu m$
Axial diffusivity
$D = 1.0\mu m^2 / ms$
Models
MONO
BI
STRETCHED
CTRW
FBTE
Intracellular compartment
S_{ic}
Extracellular compartment
S_{ec}
Tissue model
$f_{ic}S_{ic} + f_{ec}S_{ec} + f_{csf}S_{csf} + f_{tw}S_{tw}$
Model parameters
D (μm²/ms)
β
μ
Mean Axon Radius
Mean Axon Radius
FBTE
Ideal signal
Noisy signal
Fitted signal
Signal
b-values

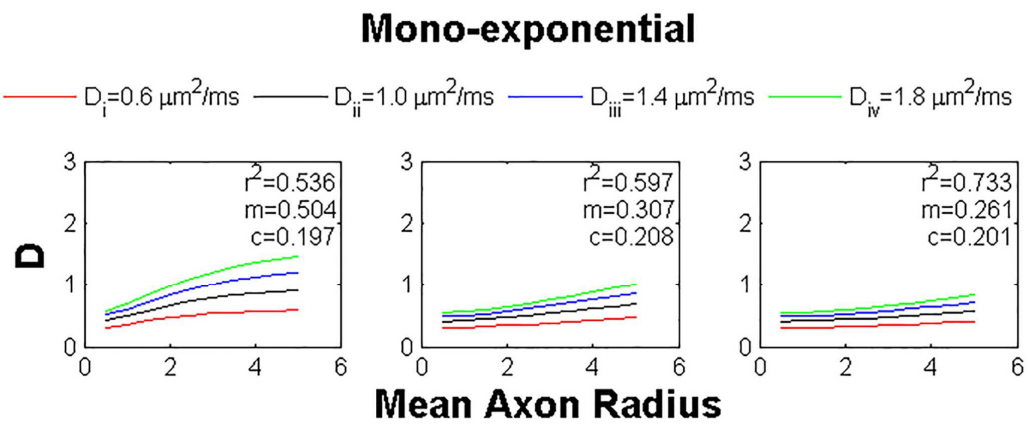

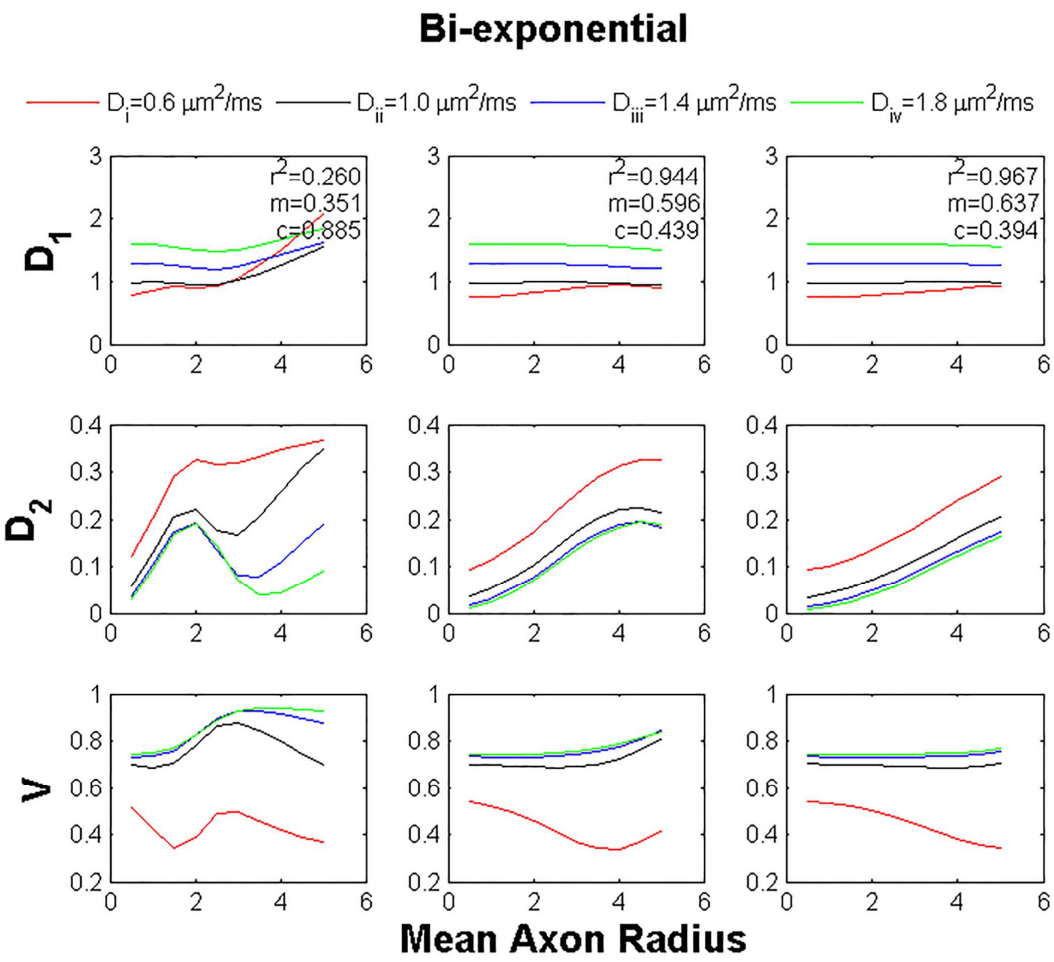
Bi-exponential
D_i=0.6 μm²/ms
D_ii=1.0 μm²/ms
D_iii=1.4 μm²/ms
D_iv=1.8 μm²/ms
r²=0.260
m=0.351
c=0.885
r²=0.944
m=0.596
c=0.439
r²=0.967
m=0.637
c=0.394
D1
D2
V
Mean Axon Radius

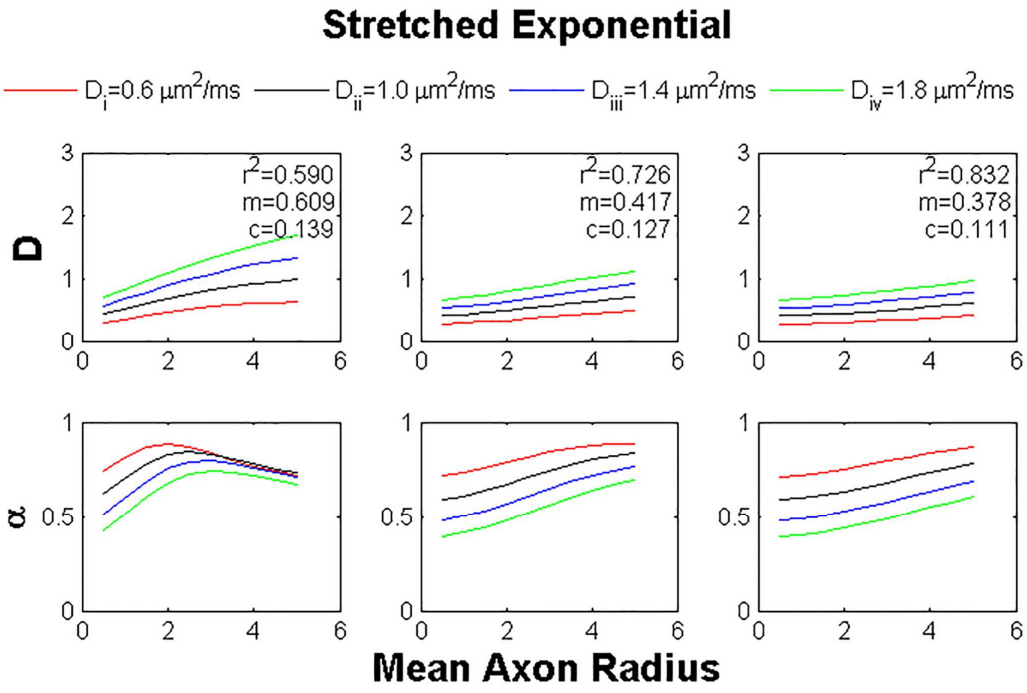

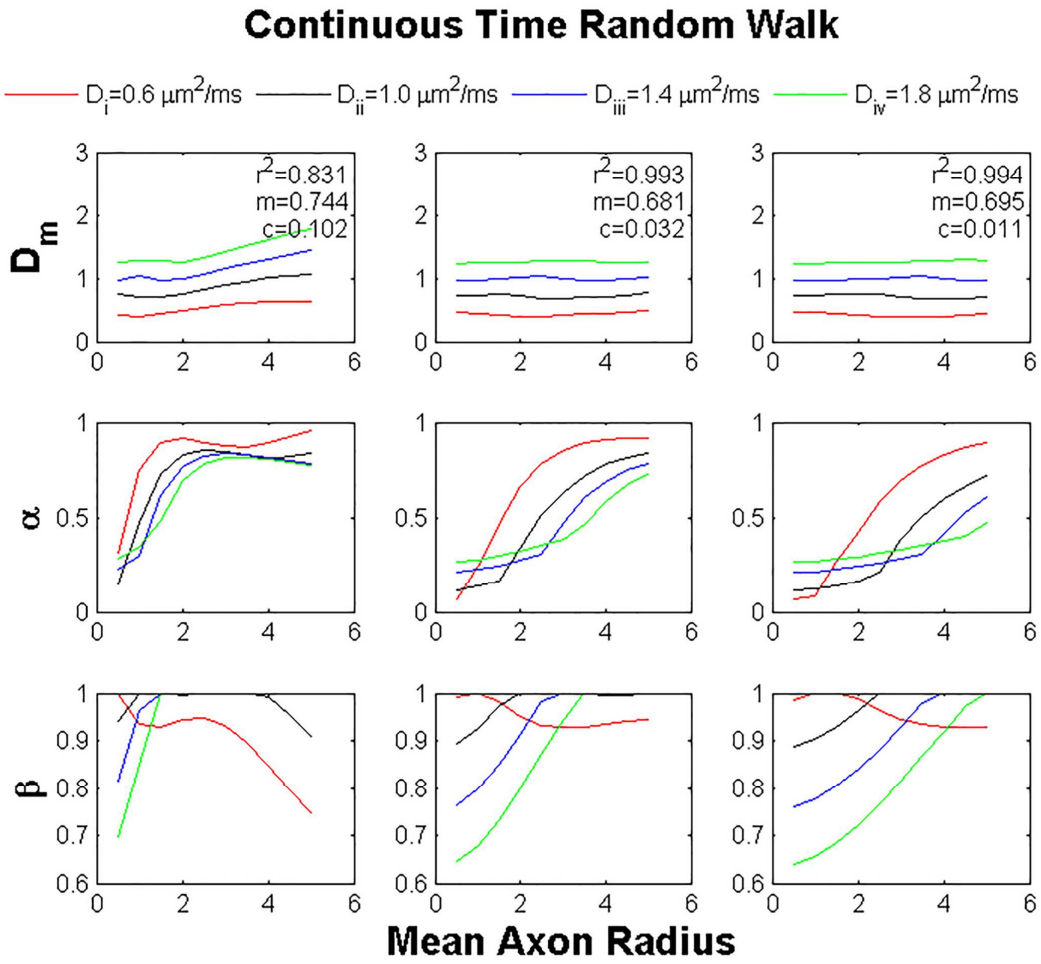
Continuous Time Random Walk
D_i=0.6 μm²/ms
D_ii=1.0 μm²/ms
D_iii=1.4 μm²/ms
D_iv=1.8 μm²/ms
D_m
α
β
r²=0.831
m=0.744
c=0.102
r²=0.993
m=0.681
c=0.032
r²=0.994
m=0.695
c=0.011
Mean Axon Radius

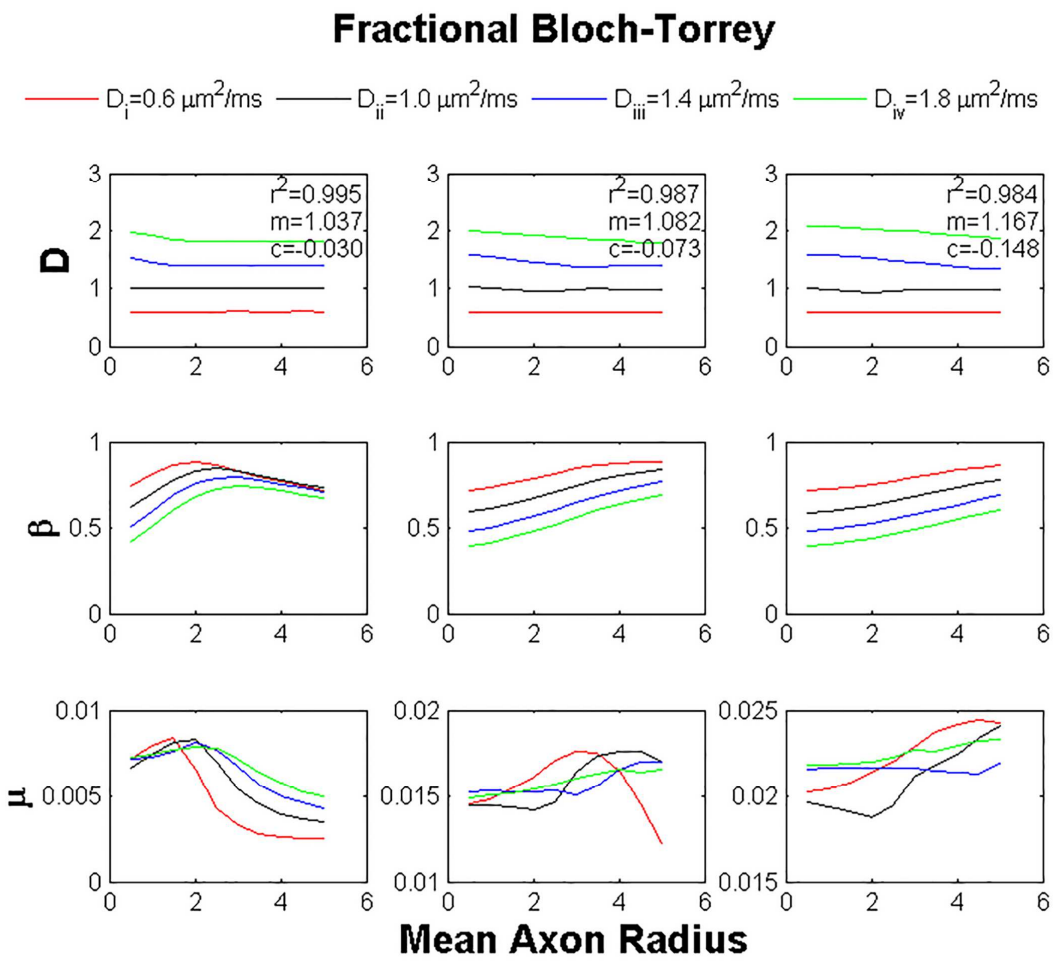
Fractional Bloch-Torrey
D_i=0.6 μm²/ms
D_ii=1.0 μm²/ms
D_iii=1.4 μm²/ms
D_iv=1.8 μm²/ms
r²=0.995
m=1.037
c=-0.030
r²=0.987
m=1.082
c=-0.073
r²=0.984
m=1.167
c=-0.148
D
β
μ
Mean Axon Radius